NeuroImage 302 (2024) 120897

Contents lists available at ScienceDirect

NeuroImage

journal homepage: www.elsevier.com/locate/ynimg

Time courses of brain plasticity underpinning visual motion perceptual learning

Yongqian Song [a,b,c], Qian Wang [a,b,d], Fang Fang [a,b,c,e,1,*]

[a] School of Psychological and Cognitive Sciences and Beijing Key Laboratory of Behavior and Mental Health, Peking University, Beijing 100871, China
[b] IDG/McGovern Institute for Brain Research, Peking University, Beijing 100871, China
[c] Peking-Tsinghua Center for Life Sciences, Peking University, Beijing 100871, China
[d] National Key Laboratory of General Artificial Intelligence, Peking University, Beijing 100871, China
[e] Key Laboratory of Machine Perception (Ministry of Education), Peking University, Beijing 100871, China

ARTICLE INFO

Keywords:
Perceptual learning
Motion
MEG
Visual cortex

ABSTRACT

Visual perceptual learning (VPL) refers to a long-term improvement of visual task performance through training or experience, reflecting brain plasticity even in adults. In human subjects, VPL has been mostly studied using functional magnetic resonance imaging (fMRI). However, due to the low temporal resolution of fMRI, how VPL affects the time course of visual information processing is largely unknown. To address this issue, we trained human subjects to perform a visual motion direction discrimination task. Their behavioral performance and magnetoencephalography (MEG) signals responding to the motion stimuli were measured before, immediately after, and two weeks after training. Training induced a long-lasting behavioral improvement for the trained direction. Based on the MEG signals from occipital sensors, we found that, for the trained motion direction, VPL increased the motion direction decoding accuracy, reduced the motion direction decoding latency, enhanced the direction-selective channel response, and narrowed the tuning profile. Following the MEG source reconstruction, we showed that VPL enhanced the cortical response in early visual cortex (EVC) and strengthened the feedforward connection from EVC to V3A. These VPL-induced neural changes co-occurred in 160–230 ms after stimulus onset. Complementary to previous fMRI findings on VPL, this study provides a comprehensive description on the neural mechanisms of visual motion perceptual learning from a temporal perspective and reveals how VPL shapes the time course of visual motion processing in the adult human brain.

1. Introduction

Visual perceptual learning (VPL) is referred to as a long-lasting improvement in performance on a visual task after training (Gibson, 1963; Fahle and Poggio, 2002). Such improvements can persist for even years (Karni and Sagi, 1993; Bi et al., 2010, 2014; He et al., 2022). Even adults, who have long passed the well-known early critical period, could benefit from VPL, demonstrating a remarkable capability to rewire their brains in response to visual experience (Watanabe and Sasaki, 2015). Therefore, VPL provides a window into the study of brain plasticity.

VPL is characterized by its specificity, with learning confined to specific attributes such as the trained location (Shiu and Pashler, 1992; Ahissar and Hochstein, 1997; Yotsumoto et al., 2008, 2009), trained eye (Karni and Sagi, 1991, 1993), and trained visual features such as orientation (Schoups et al., 1995; Schoups et al., 2001; Raiguel et al., 2006) and motion direction (Ball and Sekuler, 1982, 1987). Such specificity implies that VPL may be mediated by neural changes in early visual areas, where neurons have relatively small receptive fields and narrow feature-selective tuning properties (Hubel and Wiesel, 1962, 1968; Luo et al., 2023). Indeed, some studies have provided evidence for this view (Schoups et al., 2001; Yan et al., 2014). Alternatively, other studies proposed that higher cortical areas associated with decision-making and attention play an important role in the neural mechanisms underlying VPL (Mukai et al., 2007; Lewis et al., 2009; Kahnt et al., 2011; Jing et al., 2021). Which brain area(s) is/are changed by VPL remains one of the most important issues in VPL.

* Corresponding author at: School of Psychological and Cognitive Sciences and Beijing Key Laboratory of Behavior and Mental Health, Peking University, Beijing 100871, China.
E-mail address: ffang@pku.edu.cn (F. Fang).
[1] Web: www.psy.pku.edu.cn/english/people/faculty/professor/fangfang/index.htm.

https://doi.org/10.1016/j.neuroimage.2024.120897
Received 30 April 2024; Received in revised form 10 October 2024; Accepted 21 October 2024
Available online 21 October 2024

VPL-induced neural modifications could be manifested in various forms, including cortical response augmentation (Furmanski et al., 2004; Yotsumoto et al., 2008; Lu et al., 2021), noise correlation reduction (Bejjanki et al., 2011; Gu et al., 2011), neural selectivity enhancement (Schoups et al., 2001; Yang, 2004; Zohary et al., 1994), and reweighting of connections between visual areas and decision-making areas (Dosher et al., 2013; Dosher and Lu, 2017). VPL may not be solely attributed to one of these modifications. For example, Chen et al. (2015) observed increased neural selectivity in V3A and optimized functional connections from V3A to intraparietal sulcus (IPS) after motion direction discrimination training, and the selectivity and connectivity increases collectively accounted for the behavioral improvements.

Functional magnetic resonance imaging (fMRI) is the most widely adopted technique to investigate where VPL occurs and what neural modifications VPL induces in human brain. However, due to the limited temporal resolution of fMRI, how VPL modulates the time course of visual processing in human brain is still largely unknown.

To fill this gap, we utilized magnetoencephalography (MEG), which offers superior temporal resolution over fMRI, to examine changes in neural activities after VPL. We trained subjects to perform a motion direction discrimination task using the same paradigm as that in Chen et al. (2015). MEG signals were recorded before, immediately after, and two weeks after training. Various data analysis methods are employed, including the neural decoding method, the inverted encoding model (IEM), and the Granger causality analysis (GCA), to explore the VPL-induced neural changes and their time courses. Our results showed that VPL increased the neural selectivity, enhanced the visual response in early visual cortex (EVC) and strengthened the feedforward connection from EVC to V3A. The increase in feedforward connection was observed in 78–104 ms after the first motion stimulus onset, indicating a change at an early stage of visual motion processing. The changes in neural selectivity and EVC response amplitude co-occurred between 160 and 230 ms post-stimulus, a period during which neural activities were correlated with behavioral performance. These changes exhibit remarkable retention two weeks after training.

2. Materials and methods

2.1. Subjects

A total of 16 subjects (4 males, 18–25 years old) participated in the study. All subjects were naïve to the purpose of the study and had never participated in any perceptual learning experiment before. They were right-handed with reported normal or corrected-to-normal vision and had no known neurological or visual disorders. They gave written, informed consent in accordance with the procedures and protocols approved by the human subject review committee of Peking University.

2.2. Stimuli and apparatus

The visual stimuli and procedures used in this study were similar to those described by Chen et al. (2015). The stimuli were random-dot kinematograms (RDKs) with 100 % coherence. All dots in an RDK moved in the same direction (luminance: 3.76 cd/ m^2; diameter: 0.1°; speed: 10°/s). At any moment, 400 dots were visible within an 8° circular aperture centered at fixation. The dots were presented against a gray background (luminance: 19.8 cd/m^2). In psychophysical tests, the stimuli were presented on a Display++ 32' monitor (Cambridge Research Systems Ltd; refresh rate: 120 Hz; spatial resolution: 1920 × 1080). The subjects viewed the stimuli from an 80-cm distance. Their heads were stabilized using a head and chin rest. In MEG tests, the stimuli were back-projected onto a translucent screen using a video projector (refresh rate: 60 Hz; spatial resolution: 1024 × 768). The subjects viewed the stimuli from a 75-cm distance. The subjects were asked to fixate at the central fixation point throughout the tests.

2.3. Designs

During the training phase, each subject underwent eight daily training sessions to perform a motion direction discrimination task at a direction of θ, which was chosen randomly from eight directions (i.e., 22.5°, 67.5°, 112.5°, 157.5°, 202.5°, 247.5°, 292.5°, and 337.5°; 0° was the rightward direction) at the beginning. Throughout the experiment, the training direction (i.e., θ) was fixed. Each daily training session comprised 27 QUEST (Watson and Pelli, 1983) staircases of 40 trials, resulting in 1080 trials per day. In a trial, two RDKs with motion directions of $\theta + \Delta\theta/2$ and $\theta - \Delta\theta/2$ were presented successively for 200 ms each and were separated by a 600-ms blank interval. The temporal order of these two RDKs was randomized. The subjects were asked to make a two-alternative forced-choice (2-AFC) judgment of the direction of the second RDK relative to the first one (clockwise or counter-clockwise). After each response, informative feedback was provided by brightening (correct response) or dimming (wrong response) the fixation point. The next trial began 1 s after the feedback. $\Delta\theta$ was varied trial by trial and controlled by the QUEST staircase to estimate the subjects' discrimination thresholds at 75 % correct. During the training phase, $\Delta\theta$ was usually less than 4°. According to the findings of Liu and Weinshall (2000), our study employed a `difficult' task, i.e., a fine discrimination task.

During the three test phases, the psychophysical and MEG tests were performed at the four motion directions, which were 0°, 30°, 60°, and 90° deviated from the trained direction, all either clockwise or counter-clockwise (hereafter referred to as 0°, 30°, 60°, and 90°). Notably, no feedback was given in the psychophysical and MEG tests. Prior to the study, the subjects practiced 10 trials per direction to become familiar with the stimuli and the experimental procedure. In the psychophysical tests, 10 QUEST staircases similar to those mentioned above were completed for each direction. The discrimination thresholds from the 10 staircases for each direction were averaged to measure the subjects' discrimination performance. The subjects' performance improvements for a direction were calculated as follows: (pre-training threshold − post-training threshold) / pre-training threshold × 100 %. After acquiring the psychophysical discrimination thresholds, we collected the MEG signals responding to the stimuli at four motion directions in eight MEG runs of 100 trials and obtained 200 trials per direction. In a trial, two RDKs with the motion directions of the test direction ± $\Delta\theta/2$ were presented successively for 200 ms each. They were separated by a 600-ms blank interval and followed by a 300-ms blank interval. The fixation point was replaced by a cross as a cue, prompting the subjects to respond. A 200–800 ms interval was added between trials. The subjects were asked to make a 2-AFC judgment (clockwise or counter-clockwise) of the second motion direction relative to the first one by pressing one of two buttons. In the MEG tests, $\Delta\theta$ was fixed as the discrimination threshold measured in the psychophysical tests and made subjects perform equally well (75 % correct) across the four motion directions and the tests.

2.4. MEG signal acquisition and preprocessing

Neuromagnetic signals were recorded continuously at 1000 samples/second using a 306-channel (204 planar gradiometers, 102 magnetometers) whole-head MEG system (Elekta-Neuromag TRIUX, Helsinki, Finland) at Peking University. Vertical and horizontal electrooculograms (EOGs) were acquired simultaneously for offline eye movement artifact rejection. The head position was tracked during the MEG recording based on a set of four head position indicator (HPI) coils placed on particular head landmarks. The raw MEG data were first processed using the temporal signal space separation (tSSS) technique implemented in MaxFilter 2.2 software (Elekta Neuromag) to compensate for the head movements and reduce the noise from the external environment (Taulu and Kajola, 2005). Further preprocessing and analyses were performed using the Brainstorm toolbox (Tadel et al., 2011)

in MATLAB (MathWorks, Inc., Natick, Massachusetts). The MEG data were visually inspected. The segments contaminated by eye blinks were removed using a peak-to-peak rejection threshold of 200 μV for the EOG. Seventy-two sensors covering the occipital lobe labeled as Occipital in the MEG data acquisition system were selected for data analyses (Ramkumar et al., 2013), except for the MEG source localization.

We used either filtered or unfiltered signals for different analyses. For the majority of the decoding analyses and the IEM analyses, we utilized a 2–40 Hz band-pass filter (zero-lag linear-phase Kaiser windowed FIR filter with a transition bandwidth of 0.5 Hz) and generated MEG epochs from −100 ms to 1100 ms relative to the first RDK onset. The epochs were then downsampled to 100 Hz and baseline corrected with the average activity during the 100-ms prestimulus interval. For decoding analyses in different frequency bands, 4–7 Hz, 8–12 Hz, 12–30 Hz, and 30–150 Hz band-pass filters were utilized for the theta, alpha, beta, and gamma bands, respectively. For the theta band, the epochs were baseline corrected with the average activity during the 300-ms prestimulus interval. In this case, a longer baseline was adopted to avoid phase distortion and baseline contamination that could be introduced by the low-frequency low-pass filters. For the alpha, beta, and gamma bands, the 100-ms prestimulus interval was used for baseline correction. The epochs were then downsampled to 200 Hz. Notably, unfiltered signals were used for the GCA because filtering may cause spurious causalities (Florin et al., 2010).

2.5. Decoding analysis

Time-resolved motion direction decoding analyses were conducted for each subject using the linear supporting vector machine (libSVM) implemented in the Neural Decoding Toolbox (Meyers, 2013) in MATLAB. We used the 72 sensors from the occipital lobe. Data from both magnetometers and gradiometers were used as features for the pattern classifier. The sensor signals were normalized before decoding.

We used data from both correct and incorrect epochs. For each test direction, there were 200 epochs, with at least 150 epochs remaining after the artifact rejection. Therefore, we randomly selected 150 epochs per direction (600 trials in total) for the decoding analyses. We then employed a five-fold cross-validation procedure. The 150 epochs were randomly divided into five sets of 30 epochs. The data from each set were averaged to yield a mean epoch. Subsequently, the classifier was trained on four of these mean epochs and tested on the remaining one. This step was repeated for five times, each time using a different mean epoch as the test set and the remaining four mean epochs as the training set. We performed this cross-validation procedure for 50 times, with each repetition requiring a new random sampling of 150 epochs per direction. Decoding accuracy was defined as the mean accuracy of these 50 repetitions.

Decoding latency was defined herein as the first time point where the decoding accuracy significantly exceeded the chance level for three consecutive time points (see also Isik et al., 2014). Two subjects did not show decoding accuracies that were significantly higher than the chance level during the whole time window before training but exhibited decoding accuracies that were significantly higher than the chance level after training; hence, their decoding latencies were not calculated.

2.6. Reconstruction of time-resolved motion direction representation

We reconstructed the neural representation of the motion directions using a method similar to that used by Mo et al. (2019). The reconstruction was based on the IEM (Sprague et al., 2018), which assumed that the instantaneous sensor responses at a single time point across epochs could be expressed as a linear combination of the responses of 12 motion direction channels (i.e., from −150° to 180° in steps of 30°):

$$B = WC,$$

where B is the matrix of sensor signals at a given time point (72 sensors-by-N epochs), W is the matrix of linear weights for the direction channels (72 sensors-by-12 channels), and C is the matrix of channel responses (12 channels-by-N epochs). The IEM analysis involved two stages: model training and model-based reconstruction. For each of the three test phases (600 epochs each), we split the epochs in half to create separate training and reconstruction sets. We pooled the training sets from the three test phases together, 900 epochs in total. The remaining half of the epochs served as the reconstruction sets, 300 epochs for Pre, Post1, and Post2, respectively.

In the model training stage, we modeled the idealized tuning in each direction channel as the half-sinusoidal function raised to the 12th power peaked at the channel's preferred direction. Hence, for each epoch in the model training sessions, the channel responses could be predicted from these idealized tuning functions. The weight matrix W was estimated as follows based on the predicted channel responses:

$$\widehat{W} = B_1 C_1^T \left(B_1 C_1^T\right)^{-1},$$

where B_1 (72 sensors-by-900 epochs) is the optimal direction pattern matrix and C_1 (12 channels-by-900 epochs) is the matrix of the predicted channel responses for the presented direction in each epoch obtained from the idealized channel tuning functions. In the model-based reconstruction stage, the weight matrix was applied to the instantaneous sensor signals of the test set to estimate the instantaneous individual channel responses, as follows:

$$C_2 = \left(\widehat{W}^T \widehat{W}\right)^{-1} \widehat{W}^T B_2,$$

where B_2 (72 sensors by 300 epochs) is the matrix of instantaneous sensor signals from each test set and C_2 (12 channels-by-300 epochs) is the matrix comprising column vectors of estimated epoch-wise channel responses. These epoch-wise vectors were then averaged, yielding one vector of channel responses for each time point. Hence, the direction information in each epoch was represented in the channel space.

We fitted the channel response profiles with a Gaussian function and calculated the FWHM bandwidths. Since the data did not allow for a reliable estimation of FWHM bandwidth at the single subject level, we employed non-parametric jackknife permutation methods to examine the FWHM bandwidth difference between test phases. The model was fit to n resamples from the data. In each resample, data from one subject were omitted, and the channel responses from the remaining n-1 subjects were averaged. The FWHM bandwidth was then estimated for the averaged channel responses. This produced n different values of FWHM bandwidth and built a jackknife sample. The values of FWHM bandwidth were then compared across the jackknife samples. Five thousand permuted samples were created by randomly recoding the test phase from which each FWHM bandwidth was taken. The actual difference between the means of the jackknife distributions was then compared to the 95th percentile of the permuted samples to test whether the probability of the measured differences between different test phases occurring by chance was smaller than 0.05.

2.7. Structural MRI acquisition and preprocessing

A high-resolution structural MRI dataset was acquired for each subject using a 3T Siemens Magnetom Prisma scanner (T1-weighted; 3D MPRAGE; TE: 30 ms; TR: 2000 ms; flip angle: 90; FOV: 224 × 224 mm^2; slice orientation: transversal; voxel size: 0.5 × 0.5 × 1 mm^3) at the Center for MRI Research at Peking University. The cortical surface of each subject was reconstructed from theT1-weighted structural images using FreeSurfer (http://surfer.nmr.mgh.harvard.edu/).

2.8. MEG source reconstruction and region-of-interest selection

The structural images were co-registered to the MEG coordinate

system using the Brainstorm toolbox and SPM8. They were then segmented and linearly normalized to a template brain in the MNI space. For each subject, a head model was generated using the overlapping spheres method (Huang et al., 1999). Subsequently, a noise covariance matrix (from −100 to 0 ms) and a data covariance matrix (from 0 to 1100 ms) were estimated from the recordings. A pre-whitening process was then conducted to scale the sensor channels based on the standard deviations observed in the baseline recordings, as obtained from the noise covariance matrix. This process aligned the units and scales of the magnetometer and gradiometer data (Engemann and Gramfort, 2015). Next, using the head model and the covariance matrices, we projected the sensor-level timeseries into a source space consisting of 15,000 vertices with a cortically constrained minimum L2-norm estimate (MNE) (Hämäläinen et al., 1993). The generated source current density was then normalized by an estimate of projected noise to calculate the dynamic statistical parametric map (dSPM) (Dale et al., 2000), which was treated as the source activity. Finally, an isotropic Gaussian kernel with a full-width-at-half-maximum (FWHM) of 5 mm was applied to the dSPM for spatial smoothing.

V1d, V1v, V2d, V2v, V3A, and IPS were identified using the atlas of Wang et al. (2015). MT+ was identified using the Broadmann Area Maps of Freesurfer. Considering the spatial resolution of MEG, we combined V1d, V1v, V2d, and V2v together, which were referred to as early visual cortex (EVC).

2.9. GCA

GCA (Granger, 1969) was performed to investigate causal interactions between the regions of interest (ROIs). The principal idea behind the GCA is that if the addition of the history of signal A improves the prediction of signal B, as compared to the prediction of signal B based on its own history alone, then signal A is said to "Granger cause'' signal B. We computed the time series for each motion direction and vertex, and averaged the time series across all vertices within each ROI. To satisfy the stationarity assumption of GCA, we used the raw data without any filters. Then the data were linearly detrended, and the temporal ensemble mean at each time point was subtracted from each trial before calculating the GC values. Based on the approaches from Ding et al. (2000) and Barnett and Seth (2014), the data were separated into sequential 200-ms sliding time windows in steps of 1 ms. Granger causality analyses were conducted independently for each time window. Time series in each window were then added into a multivariate autoregressive (MVAR) model to calculate GC values. The model order, a parameter indicating the number of time lags required to estimate the MVAR model, was determined using the Akaike information criterion (Akaike, 1974).

2.10. Statistical analyses

Bonferroni correction was applied with *t*-tests, correlations, and ANOVAs involving multiple comparisons. Before performing ANOVAs, we first verified the data distribution assumptions of normality and heteroscedasticity using the Shapiro–Wilk and Levene's tests, respectively.

For the decoding analyses, we utilized a nonparametric permutation test to determine whether or not the decoding accuracies significantly exceeded the chance levels and calculate the decoding latencies. We generated a null distribution by running the decoding procedure for 200 times with randomly shuffled labels. Decoding accuracies that exceeded all points in the null distribution for the corresponding time point were deemed significant with $p < 0.005$ (1/200).

A similar nonparametric permutation test was conducted for the Granger causality analyses. The Granger causality (GC) values were calculated by shuffling the time series for 10 times. Subsequently, we combined the GC values for all time points to form a null distribution and used GC values above 95 % of the points in this distribution as the significance criteria.

To avoid an inflated family-wise error rate, we employed cluster-based permutation tests when conducting within-group comparisons of time courses of the decoding accuracy and the Granger causality before and after training. This approach searches for temporal clusters of individually significant time points by taking advantage of the fact that information is typically distributed over the adjacent time points but does not require any assumptions about normality.

To implement this approach, we first applied paired t tests to determine whether or not the decoding accuracy at each time point became significantly higher after training. We then identified the clusters of the consecutive time points for which the t tests were significant ($p < 0.05$) and computed the cluster-level *t mass* (i.e., sum of the *t* scores within each cluster). Subsequently, we evaluated if the computed *t mass* of a cluster was larger than what could be expected by chance, which was determined through permutation tests. This strategy controlled the Type-I error rate at the cluster level, yielding a probability of 0.05 that one or more clusters will be significant if training did not influence the decoding accuracy. We then constructed a null distribution of the cluster-level *t mass* values through the permutation tests. In this process, we randomly permuted the test labels (Pre/Post) for each subject and calculated the *t* values in the same manner as that for the original nonpermuted data. For each permutation, the largest *t* mass value was recorded and added to the permuted distribution. This permutation process was iterated for 5000 times to generate a null distribution. The *p* value for each cluster in the actual data set was determined based on the nearest null distribution percentiles. We rejected the null hypothesis and inferred a training effect on the decoding accuracy if the observed *t mass* value for a given cluster fell within the top 5 % of the null distribution. The procedures for comparisons of Granger causality were conducted in the same manner.

3. Results

3.1. Behavioral results

We first applied a repeated-measures ANOVA to the motion direction discrimination thresholds measured at Pre, with motion direction (0°, 30°, 60°, and 90°) as a within-subject factor. The main effect of motion direction was not significant (F (3,45) = 1.951, p = 0.135), demonstrating no significant difference in motion direction discrimination performance between the motion directions before training (Fig. 1).

As shown in Fig. 2A, the motion direction discrimination thresholds gradually decreased throughout the training. The thresholds measured during the training phase were submitted to a repeated-measures ANOVA with a within-subject factor of training day. The main effect of training day was significant (F (7, 105) = 12.185, $p = 2.57 \times 10^{-11}$). We then conducted another repeated-measures ANOVA to the motion direction discrimination thresholds measured at test phases with test (Pre, Post1, and Post2) and motion direction (0°, 30°, 60°, and 90°) as within-subject factors. Both the main effects of test (F (2,14) = 20.589, $p = 6.8 \times 10^{-5}$) and motion direction (F (3,13) = 20.589, $p = 5.74 \times 10^{-4}$) were significant. The interaction between the test and motion direction was significant (F (6,10) = 8.028, p = 0.00232). Bonferroni corrected post hoc *t*-tests showed that the thresholds for the trained direction were significantly lower at Post1 (t (15) = 9.015, $p = 3.84 \times 10^{-7}$) and Post2 (t (15) = 10.417, $p = 5.83 \times 10^{-8}$) compared with those at Pre, suggesting a significant and long-lasting learning effect for the trained direction (Fig. 2B).

We then calculated the percent improvement in discrimination performance, revealing over 50 % improvement at both Post1 and Post2 for the trained direction. We also conducted another repeated-measures ANOVA to the percent improvements, with test (Post1 and Post2) and direction (0°, 30°, 60°, and 90°) as within-subject factors. Neither the main effect of test (F (1, 15) = 0.047, p = 0.832) nor the interaction between test and direction (F (3,45) = 1.238, p = 0.307) was significant.

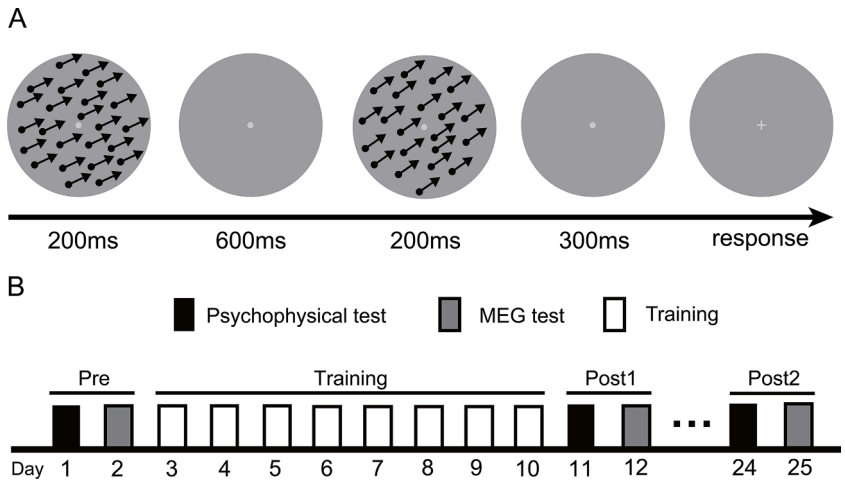

Fig. 1. Stimuli and experimental protocol. (A) Schematic description of a two-alternative forced-choice (2-AFC) trial in a QUEST staircase for measuring motion direction discrimination thresholds. Subjects were asked to judge the direction of the second RDK relative to the first one (clockwise or counterclockwise). (B) Experimental protocol. The subjects underwent motion direction discrimination training at a fixed motion direction over eight days with 1080 trials per day. They were tested at 0°, 30°, 60°, and 90° away from the trained direction on the days before (Pre), immediately after (Post1), and two weeks after training (Post2).

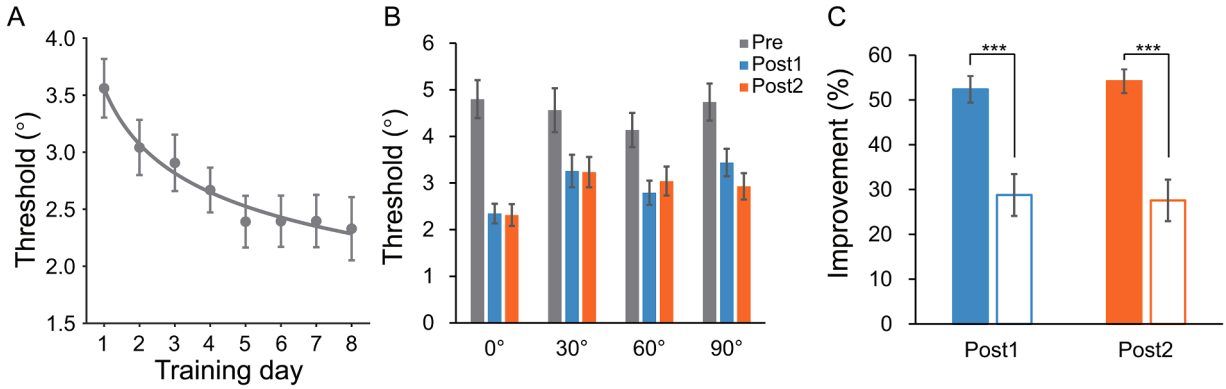

Fig. 2. Perceptual learning effects. (A) Learning curve. Motion direction discrimination thresholds are plotted as a function of training day. (B) Motion direction discrimination thresholds at Pre, Post1, and Post2. (C) Percent improvements in motion direction discrimination performance for the trained (solid bar) and untrained (hollow bar) directions at Post1 and Post2 relative to those at Pre. No significant difference was found between the three untrained directions (30°, 60°, and 90°); hence, the improvements for these directions were averaged. Asterisks indicate significant differences between the improvements for the trained and untrained directions (***$p < 0.001$). Error bars denote 1 SEM calculated across the subjects.

By contrast, the main effect of direction was highly significant (F (3,45) = 12.095, $p = 6 \times 10^{-6}$). Bonferroni corrected post hoc t-tests revealed a higher improvement for the trained direction compared to that for the three untrained directions (0° vs. 30°, t (31) = 5.540, $p = 3.4 \times 10^{-4}$; 0° vs. 60°, t (31) = 4.862, $p = 1.2 \times 10^{-3}$; 0° vs. 90°, t (31) = 5.010, $p = 9.3 \times 10^{-4}$), indicating a strong learning specificity. Meanwhile, no significant difference in percent improvement was found between the three untrained directions (all $p > 0.05$).

3.2. Decoding results

We used a multivariate decoding approach to classify the occipital MEG signals elicited by the trained and untrained directions in a time-resolved manner at Pre, Post1, and Post2. If training refines the neural representations of the motion directions, and therefore, renders the representations more discriminable, the decoding accuracy will increase after training. Meanwhile, the time when the increase in decoding accuracy occurs could inform us how VPL modifies the time course of visual motion processing.

First, in a four-way motion direction (0°/30°/60°/90°) decoding analysis, we compared the time courses of decoding accuracies at Pre and Post1/Post2. As shown in Fig. 3A, training-induced increases in decoding accuracy at Post1 were observed during 150–340 ms after the first RDK onset ($p < 1 \times 10^{-10}$, cluster-based permutation test) and during 160–230 ms after the second RDK onset ($p = 0.034$, cluster-based permutation test). At Post2, increased decoding accuracies were found both after the first RDK onset (140–210 ms, $p = 0.0390$; 240–310 ms, $p = 0.0070$; 380–500 ms, $p = 0.0176$; cluster-based permutation test) and the second RDK onset (90–230 ms, $p = 0.0002$, cluster-based permutation test). Therefore, the time windows with increased decoding accuracies at Post1 and Post2 overlapped, that is, 150–210 ms and 240–310 ms after the first RDK onset and 160–230 ms after the second RDK onset. No difference was found between Post1 and Post2 at all time points (all $p > 0.05$, cluster-based permutation test). To test whether there is a global time effect, we conducted a repeated-measures ANOVA on the decoding accuracy at each time point with test time as the within-subject factor. To avoid an inflated family-wise error rate, we employed FDR correction on the ANOVA results. The main effect of test time was significant during 160–200 ms, 250–310 ms, and 470–490 ms after the first RDK and during 100–120 ms, 160–220 ms, and 270–280 ms after the second RDK.

The peak decoding accuracies for the first RDK at Post1 (t (15) = 5.502, $p = 0.0001$) and Post2 (t (15) = 4.445, $p = 0.0009$) were significantly higher than that at Pre (Fig. 3B). Notably, we found

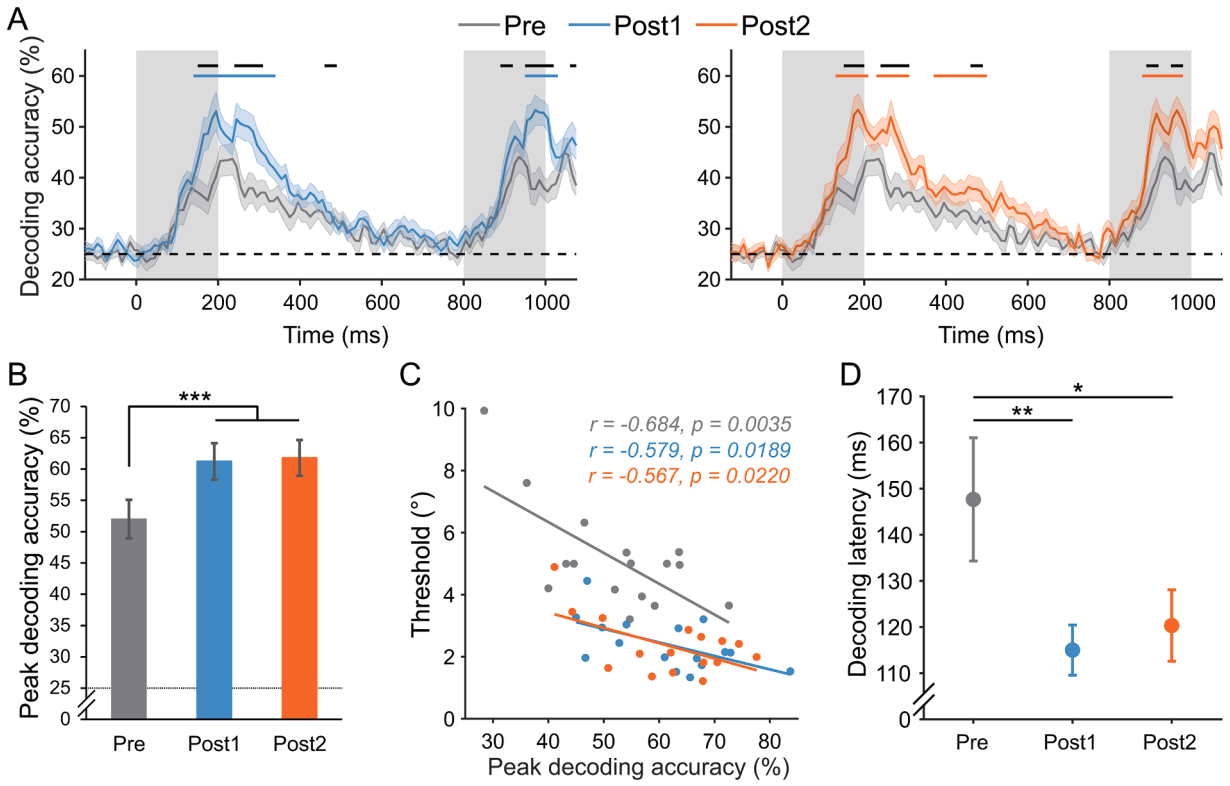

Fig. 3. Four-way decoding results. (A) Time courses of decoding accuracy at Pre, Post1, and Post2. The shaded areas around the time courses indicate the standard error of the mean. The gray rectangular areas depict the stimulus presentation intervals. T The blue (Post1) / orange (Post2) lines on the top represent the time periods with significant decoding accuracy increases after training. The black lines on the top represent the time periods with the significant main effect of test in the ANOVA. The dashed lines indicate the chance level of the four-way decoding analysis (25 %). (B) Peak decoding accuracies for the first RDK at Pre, Post1, and Post2. Asterisks indicate significant increases in peak decoding accuracy after training (***$p < 0.001$). (C) Correlations between the peak decoding accuracies and the motion direction discrimination thresholds at Pre, Post1, and Post2. (D) Decoding latencies at Pre, Post1, and Post2. Asterisks indicate significant decreases in decoding latency after training (*$p < 0.05$, **$p < 0.01$). Error bars denote 1 SEM calculated across the subjects.

significant correlations between the peak decoding accuracies for the first RDK and the thresholds at Pre (*Pearson's* $r = -0.684$, $p = 0.0035$), Post1 (*Pearson's* $r = -0.579$, $p = 0.0189$), and Post2 (*Pearson's* $r = -0.567$, $p = 0.0220$) (Fig. 3C). Furthermore, the decoding latencies at Post1 (115.00 ± 5.43 ms) and Post2 (120.33 ± 7.74 ms) were significantly shorter than that at Pre (147.67 ± 13.36 ms; Post1 vs. Pre, $t(14) = 3.361$, $p = 0.0093$; Post2 vs. Pre, $t(14) = 2.927$, $p = 0.0221$), indicating that training might speed up the visual processing of the motion direction, and maintained for at least two weeks (Fig. 3D). Therefore, the decoding accuracy findings not only captured individual differences in the motion direction discrimination but also reflected the training-induced acceleration in the visual motion processing and refinement in the neural representation of the motion direction.

It could be argued that the improved decoding accuracies in the four-way decoding analysis could be attributed to the refined neural representation of the trained direction or some untrained direction(s). To examine this issue, we performed two two-way decoding analyses −0° vs. 30° classification and 60° vs. 90° classification. We hypothesize that if training only refines the neural representation of the trained direction, we should observe an improved decoding accuracy with the 0° vs. 30° classification but not with the 60° vs. 90° classification.

The decoding accuracy for the 0° vs. 30° classification (Fig. 4A) at Post1 was significantly higher than that at Pre during 150–200 ms after the first RDK onset ($p = 0.0266$, cluster-based permutation test) and was also evident during 150–210 ms after the second RDK onset ($p = 0.0420$, cluster-based permutation test). At Post2, decoding accuracy increases were observed during 140–190 ms after the first RDK onset ($p = 0.0342$, cluster-based permutation test). Therefore, the time window during which decoding accuracies increased at Post1 and Post2 overlapped during 150–190 ms after the first RDK onset. No difference was found between Post1 and Post2 at all time points (all $p > 0.05$, cluster-based permutation test). Repeated-measures ANOVA revealed significant main effect of test time during 160–200 ms, 240–260 ms, and 330–340 ms after the first RDK and during 160–200 ms after the second RDK, suggesting a global time effect of training.

The peak decoding accuracies at Post1 ($t(15) = 3.885$, $p = 0.003$) and Post2 ($t(15) = 2.422$, $p = 0.057$) also increased (Fig. 4B). Similar to the four-way decoding analyses, the neural decoder performance paralleled the behavioral performance because significant correlations were observed between the peak decoding accuracies and the thresholds at Pre (*Pearson's* $r = -0.694$, $p = 0.0029$), Post1 (*Pearson's* $r = -0.465$, $p = 0.0696$), and Post2 (*Pearson's* $r = -0.569$, $p = 0.0214$) (Fig. 4C). Compared with the decoding latency at Pre (157.08 ± 12.30 ms), the latencies at Post1 (136.67 ± 11.22 ms) and Post2 (131.67 ± 10.02 ms) were also shorter (Post1 vs. Pre, $t(11) = 3.478$, $p = 0.0103$; Post2 vs. Pre, $t(11) = 3.056$, $p = 0.0218$)(Fig. 4D). On the contrary, for the 60° vs. 90° classification, we failed to find a decoding accuracy increase and a decoding latency reduction (Fig. 4E–H). In summary, the two-way decoding analysis results support our hypothesis that training augments the differentiation of the neural representation around the trained direction and speeds up the visual motion processing of the trained direction, echoing our four-way decoding findings.

To examine which frequency band in the MEG signals contributed to the improved decoding accuracy, we performed the decoding analysis at the frequency bands of theta, alpha, beta, and gamma. For theta band, learning effects appeared during 150–450 ms after the first RDK onset at Post1 ($p < 1 \times 10^{-10}$, cluster-based permutation test) and during 150–460 ms after the first RDK onset at Post2 ($p < 1 \times 10^{-10}$, cluster-

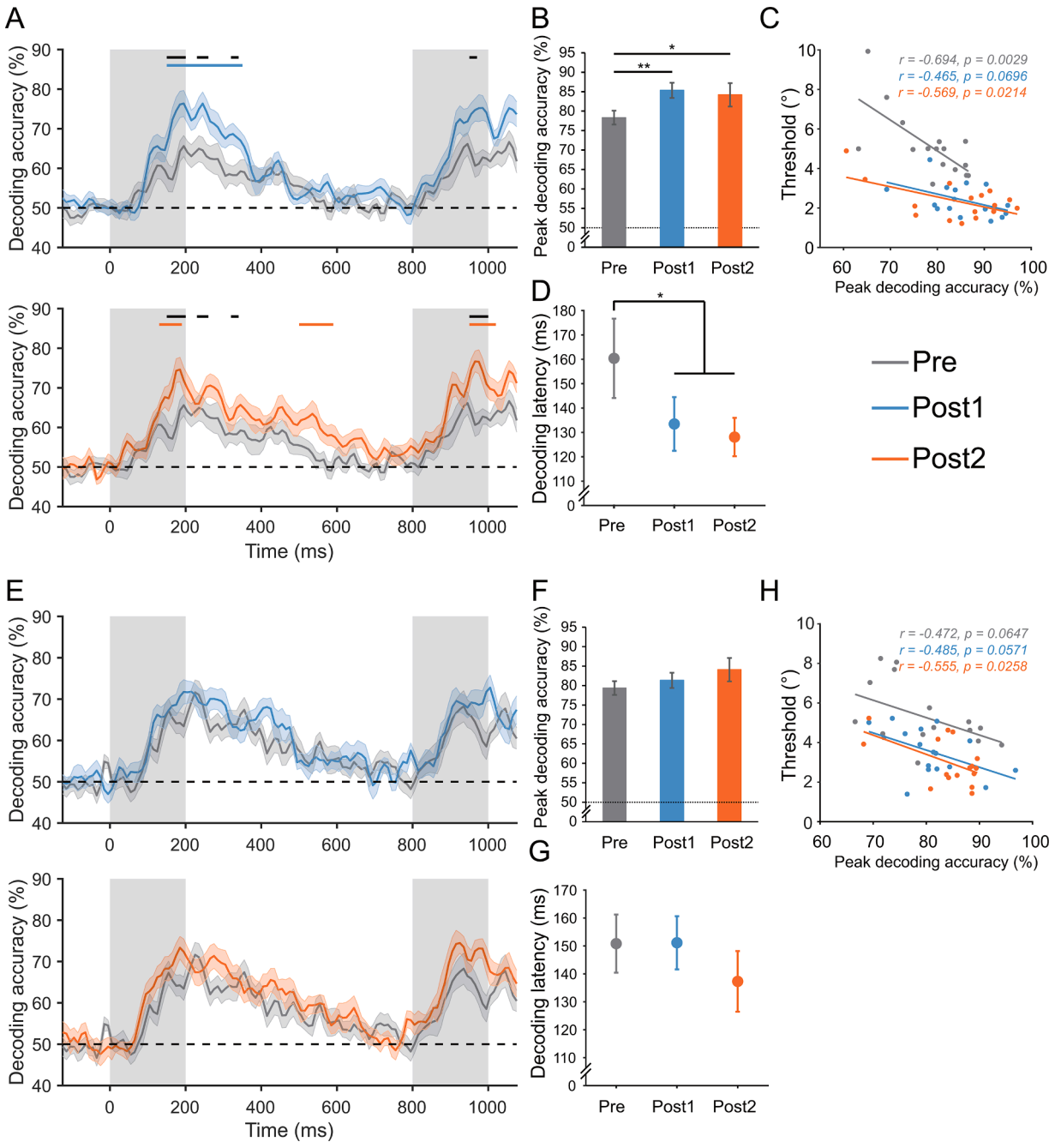

Fig. 4. Two-way decoding results around the trained (0° vs. 30°, A-D) and untrained (60° vs. 90°, E-H) directions and plotted in the same format as in Fig. 3. Error bars denote 1 SEM calculated across the subjects. Asterisks indicate significant decreases in decoding latency after training and significant increases in peak decoding accuracy after training (*$p < 0.05$, **$p < 0.01$).

based permutation test) (Fig. 5A). Therefore, these two intervals overlapped at 150–450 ms after the first RDK onset, which is consistent with the time window of the learning effect observed in the previous broadband signal decoding analyses. Similarly, the peak decoding accuracy of the theta band signals increased significantly at Post1 (t (15) = 3.919, p = 0.0164) and Post2 (t (15) = 5.023, p = 0.0018). For other frequency bands, no significant learning-induced changes in decoding accuracy were detected (Fig. 5B–D).

3.3. IEM

We then examined how and when VPL would modify the neural selectivity for the trained RDK. Herein, we utilized the IEM to decompose the MEG sensor signals into 12 hypothetical direction-selective channel responses and reconstruct the channel responses to the trained and untrained (i.e., 90°) RDKs.

First, we averaged the responses for each channel between 0 and 400 ms after the first RDK onset (Fig. 6B). Training significantly enhanced the channel responses to the trained RDK at both Post1 and Post2 primarily in the channels tuned to the trained direction (Post1:t (15) = 6.209, $p = 2.04 \times 10^{-4}$; Post2:t (15) = 5.518, $p = 7.08 \times 10^{-4}$) and surrounding directions, including the −30° offset (Post1:t (15) = 5.384, $p = 9.12 \times 10^{-4}$; Post2:t (15) = 5.511, $p = 7.20 \times 10^{-4}$) and the +30° (Post1:t (15) = 4.109, p = 0.011) offset. No significant response change occurred in any channel for the untrained direction (all $p > 0.05$, Fig. 6D).

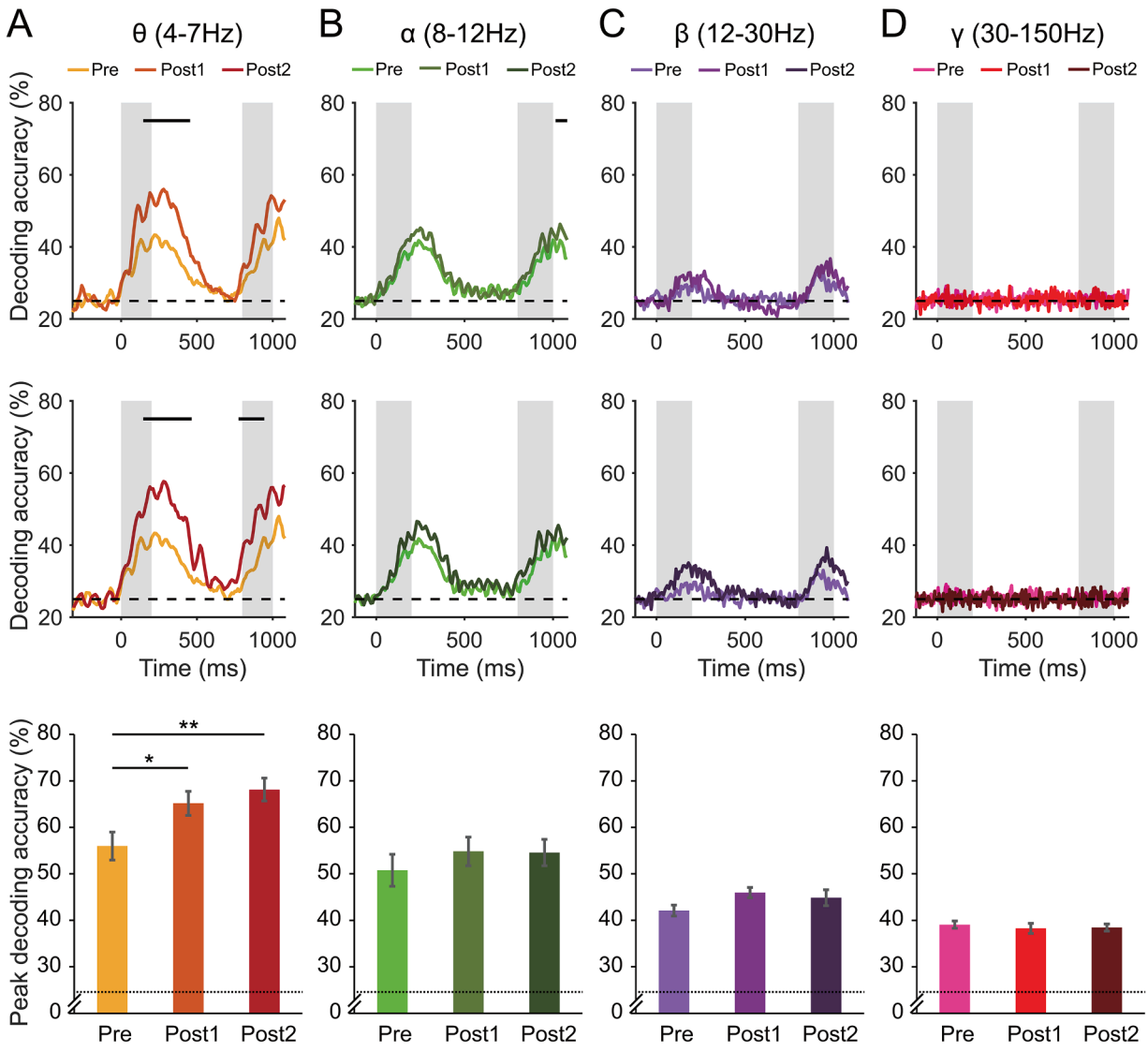

Fig. 5. Four-way decoding results in different frequency bands: theta (A), alpha (B), beta (C), and gamma (D). Top: time courses of the decoding accuracy at Pre and Post1. The gray rectangular areas indicate the stimulus presentation intervals. The black lines on the top represent the time periods with significant increases in decoding accuracy after training. The dashed lines denote the chance level of the four-way decoding analysis (25 %). Middle: time courses of decoding accuracy at Pre and Post2. Bottom: peak decoding accuracies for the first RDK at Pre, Post1, and Post2. Asterisks indicate a significant increase in decoding accuracy after training (*$p < 0.05$, **$p < 0.01$). Error bars denote 1 SEM calculated across the subjects.

Next, we fitted the channel response profiles with a Gaussian function and calculated its FWHM bandwidth as a measurement of neural selectivity. For the trained RDK, the FWHM bandwidth was significantly smaller at Post1 (Post1 vs. Pre, $p = 0.0092$, jackknife permutation test) and Post2 (Post2 vs. Pre, $p = 0.0213$, jackknife permutation test) than that at Pre. No bandwidth difference was found when viewing the untrained RDK (Post1 vs. Pre, $p = 0.1418$; Post2 vs. Pre, $p = 0.2603$; jackknife permutation test).

To investigate when the tuning change emerged, we calculated the average channel responses for the trained RDK within consecutive 50 ms time windows, starting from the onset of the first RDK (Fig. 6E). We then submitted the responses of the channel tuned to the trained direction to a repeated-measures ANOVA with time window and test as within-subject factors. Significant main effects of test (F (2,30) = 17.55, $p = 9 \times 10^{-6}$) and time window (F (7105) = 16.63, $p < 1 \times 10^{-10}$) were observed. Training enhanced channel response during the time windows of 150–200 ms, 200–250 ms, 300–350 ms, and 350–400 ms (see Table 1). Narrowed FWHM bandwidths after training were also observed at Post1 (150–200 ms, $p = 0.0321$; 200–250 ms, $p = 0.0023$; 300–350 ms, $p = 0.0316$; 350–400 ms, $p = 0.0152$; jackknife permutation test) and Post2 (150–200 ms, $p = 0.0413$; 200–250 ms, $p = 0.0345$; 300–350 ms, $p = 0.0284$; 350–400 ms, $p = 0.013$; jackknife permutation test) (Fig. 6F). Therefore, the learning-induced changes in the cortical tuning and decoding accuracy occurred within the same time period.

3.4. Cortical activities and GCA

The IEM reconstruction estimated the hypothetical direction-selective channel responses to the RDKs. To directly quantify cortical activities to the trained and untrained RDKs, we mapped MEG sensor maps to cortical sources using a dSPM approach. We selected four ROIs: EVC, V3A, MT+, and IPS, and calculated the time series of normalized response within each ROI.

Only in EVC we found VPL-induced increase in cortical response to the trained RDK (Fig. 7A). This increase was observed at both Post1 (168–234 ms, $p = 0.0002$; 966–1034 ms, $p < 1 \times 10^{-10}$; cluster-based permutation test) and Post2 (180–223 ms, $p = 0.0092$; 973–1022 ms, $p = 0.0118$; cluster-based permutation test). No other ROI exhibited

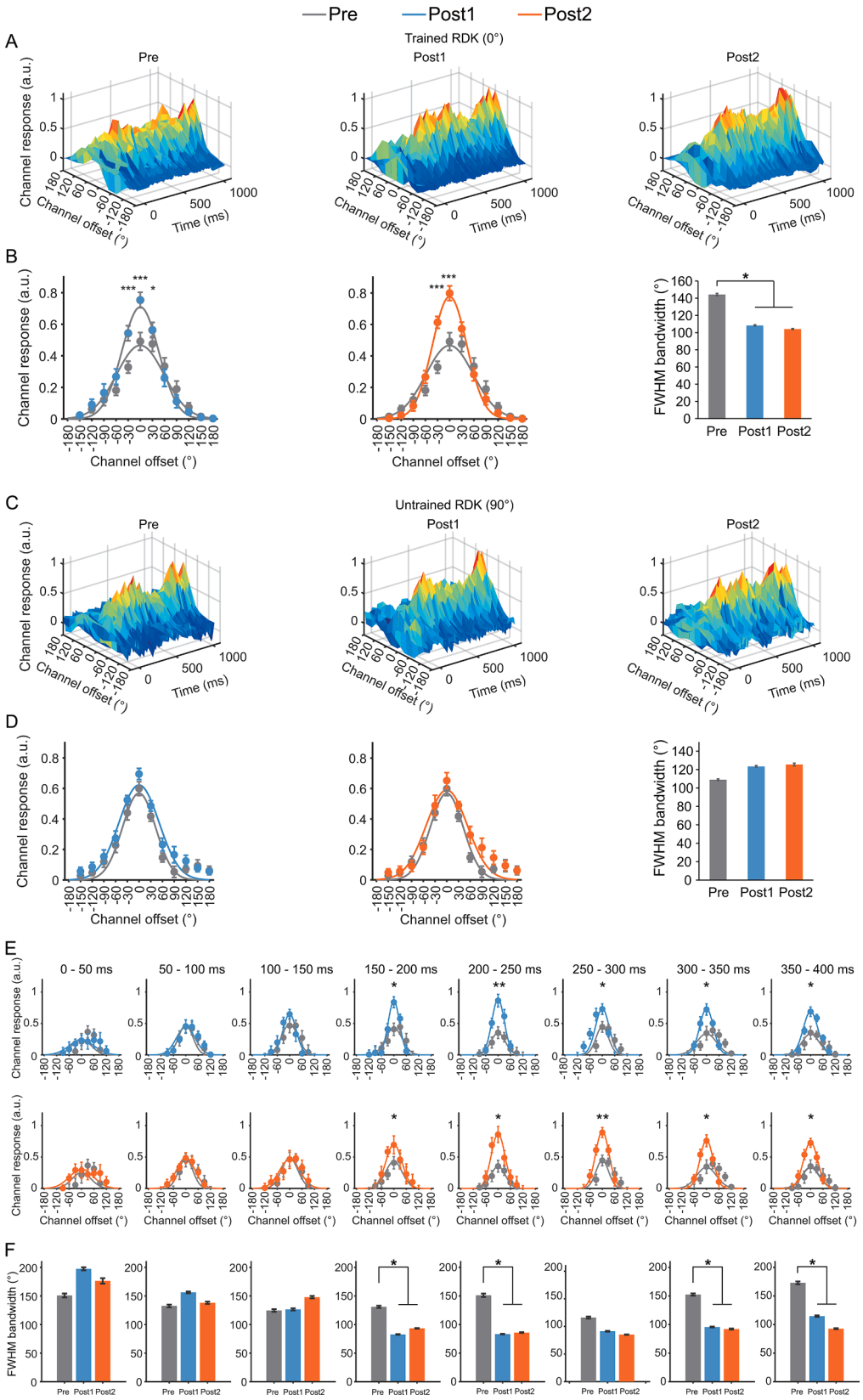

Fig. 6. IEM results. (A and C) Reconstructed channel responses during the visual processing of the trained RDK (0°) and the untrained RDK (i.e., 90°) at Pre, Post1, and Post2. (B and D) Left and middle: channel responses to the trained RDK and the untrained RDK averaged over the 0–400 ms time window at Pre, Post1, and Post2. Asterisks denote significant increases in channel response after training (*$p < 0.05$, ***$p < 0.001$). Right: FWHM bandwidths of the fitted curves for channel response profiles. Asterisks denote significant decreases in the FWHM bandwidths (*$p < 0.05$). (E) Channel responses to the trained RDK averaged for each 50 ms time window. Asterisks denote significant increases in channel response after training (*$p < 0.05$, **$p < 0.01$). (F) FWHM bandwidths of the fitted curves for each time window. Error bars denote 1 SEM calculated across the subjects. Asterisks denote significant decreases in FWHM bandwidth after training (*$p < 0.05$, **$p < 0.01$).

Table 1
Significant training-induced changes in channel response to the trained RDK, averaged within each 50 ms time window (*$p < 0.05$, **$p < 0.01$).

Time window (ms)	Post1 vs. Pre		Post2 vs. Pre	
	T-value ($df = 15$)	*p*-value	*T*-value ($df = 15$)	*p*-value
150–200	2.658	0.036*	2.758	0.029*
200–250	3.650	0.005**	2.765	0.029*
250–300	2.644	0.037*	3.567	0.006**
300–350	3.263	0.010*	3.070	0.016*
350–400	3.067	0.016*	3.122	0.014*

significant change in response after training. For the untrained RDK, no change was found in any ROI. For the averaged response between 0 and 400 ms, only the response in EVC increased after training (Post1 vs. Pre, t (15) = 4.381, p = 0.0011; Post2 vs. Pre, t (15) = 3.467, p = 0.0066) (Fig. 7B).

Next, we examined the training-induced feedforward and feedback connection changes among these ROIs. Accordingly, we calculated the directional GC between the pairwise combinations of EVC, V3A, MT+, and IPS, using a 200 ms sliding window.

The results showed that training increased the feedforward connection from EVC to V3A for the trained direction at both Post1 (78–104 ms, $p < 1 \times 10^{-10}$; 143–181 ms, $p < 1 \times 10^{-10}$; 795–819 ms, p = 0.0016; 1020–1068 ms, $p < 1 \times 10^{-10}$; cluster-based permutation test) and Post2 (75–104 ms, $p < 1 \times 10^{-10}$; 134–205 ms, $p < 1 \times 10^{-10}$; 210–230 ms, p = 0.0392; 439–462 ms, p = 0.0026; cluster-based permutation test) (Fig. 8A, top panels). Therefore, the time windows with increased feedforward connection at Post1 and Post2 overlapped, that is, 75–104 ms and 143–181 ms after the first RDK onset. Notably, the connection increase was also specific to the trained direction (Fig. 8A, bottom panels). No other ROI pair exhibited reliable, consistent feedback and/or feedforward connection changes across Post1 and Post2. Fig. 8B depicts the averaged GC values between 0 ms and 400 ms after the first RDK onset. Only the feedforward connection from EVC to V3A increased after training (Post1 vs. Pre, t (15) = 1.853, p = 0.0417; Post2 vs. Pre, t (15) = 2.428, p = 0.014).

4. Discussion

This study presents several key findings. VPL (1) increased the motion direction decoding accuracy, (2) reduced the motion direction decoding latency, (3) enhanced the direction-selective channel response and narrowed the tuning profile estimated by the IEM, (4) enhanced the EVC response, and (5) strengthened the feedforward connection from EVC to V3A. These changes were only found in the visual processing of the trained direction, demonstrating the specificity of VPL-induced neural changes. The increase in feedforward connection was observed during 78–104 ms after the first RDK onset. Other changes co-occurred during 160–230 ms after the first RDK onset.

Our results suggest that VPL increased the neural selectivity for the trained direction. This was evident in the increased decoding accuracy and the narrowed tuning profile estimated by the IEM. The VPL-induced increase in decoding accuracy has been found in EVC (Yan et al., 2014; Zhang et al., 2023), MT+ (Chen et al., 2017), and V3A (Shibata et al., 2012; Chen et al., 2015). Such an increase suggested that the neural representation of the trained direction became more separated from

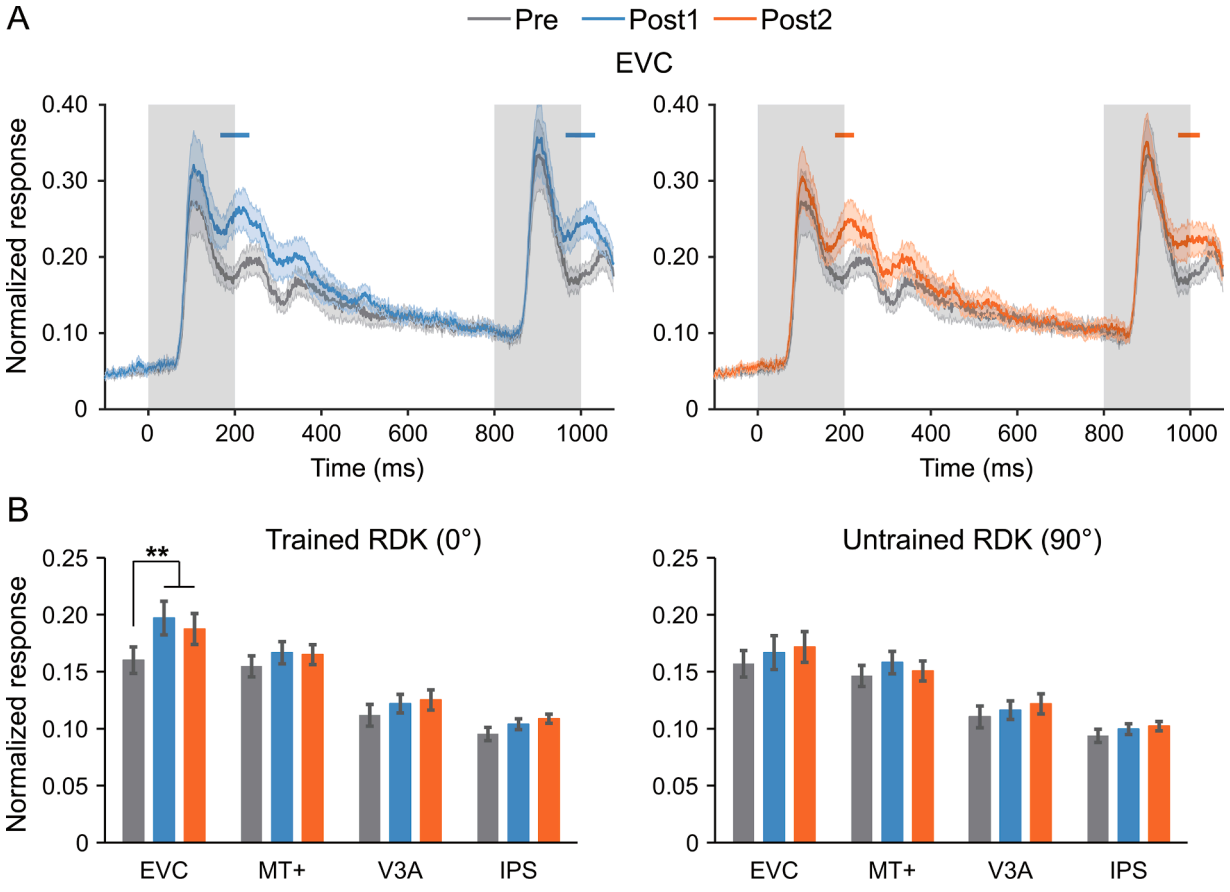

Fig. 7. Cortical activities. (A) Early visual cortex (EVC) responses to the trained RDK at Pre, Post1, and Post2. The shaded areas around the time courses indicate the standard error of the mean. The gray rectangular areas depict the stimulus presentation intervals. The blue (Post1) / orange (Post2) lines on the top represent the time periods with significant cortical activity increases after training. (B) Averaged responses to the trained RDK and the untrained RDK (i.e., 90°) from 0 to 400 ms in EVC, V3A, MT+, and IPS. Asterisk indicates significant increases in response after training (**$p < 0.01$). Error bars denote 1 SEM calculated across the subjects.

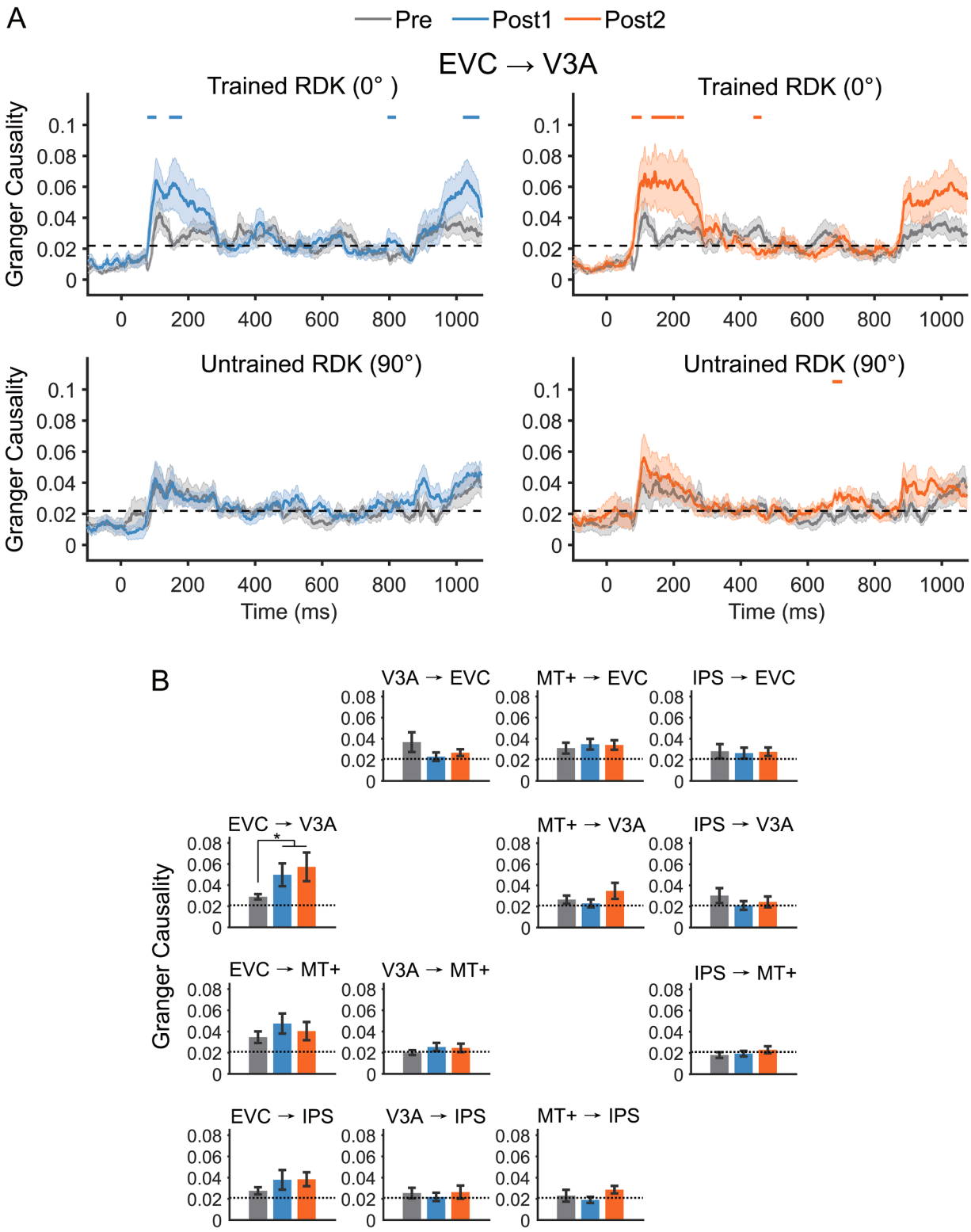

Fig. 8. Granger causality analysis (GCA) results. (A) The top panels show the time courses of directional GC from early visual cortex (EVC) to V3A during the visual processing of the RDKs for the trained direction, while the bottom panels depict those for the untrained direction (i.e., 90°), measured at Pre, Post1, and Post2. The GC value at each time point was calculated within a time window that extended 200 ms before the time point. The shaded areas around the time courses depict the standard error of the mean. The blue (Post1) / orange (Post2) lines on the top indicate the time periods with significant increases in GC value after training. The dashed lines indicate the GC value at the 95th percentile of the null distribution calculated using a random shuffle method. (B) Averaged directional GC values for the trained RDK from 0 ms to 400 ms after the first RDK onset. The GC values were calculated between the pairwise combinations of EVC, V3A, MT+, and IPS. The asterisk indicates significant increases in GC value after training (*$p < 0.05$). Error bars denote 1 SEM calculated across the subjects.

those of the untrained directions after VPL. This speculation could be further supported by the narrowed FWHM bandwidth of cortical tuning. For the trained direction, the channel response profile became steeper after VPL, making it easier to discriminate the trained direction from the other directions.

Another change in the IEM channel response profiles was the enhancement in response amplitude for the channels preferring the trained direction and its neighboring directions. This is consistent with previous studies that showed the neural augmentation induced by VPL (Bao et al., 2010; Furmanski et al., 2004; Hua et al., 2010; Larcombe et al., 2018; Schwartz et al., 2002). One could argue that the enhancement in channel response, estimated with the IEM, does not necessarily reflect corresponding changes in real cortical responses to the RDKs. To address this issue, following the MEG source reconstruction, we estimated the cortical responses to the trained RDK in EVC, MT+, V3A, and IPS. As a result, we observed an increase in EVC response to the trained RDK. The increase remained two weeks after training, demonstrating a persistent change.

We attempted to decode the motion directions from theta, alpha, beta, and gamma band MEG signals. Only in theta band (4–7 Hz) did we find increased decoding accuracy after training. Bastos et al. (2015) and Spyropoulos et al. (2018) demonstrated that the feedforward information in the primate visual system is conveyed through theta (~4 Hz)- and gamma (~60–80 Hz)-band synchronization. Kienitz et al. (2021) found that in V1, both theta and gamma oscillations occurred primarily in the supragranular layers, which serve as the cortical output compartment of V1. In addition, when major feedforward input to V4 was removed by lesioning V1, the V4 theta was eliminated. Therefore, we speculate that the increase in decoding accuracy might be relevant to the change in feedforward transmission of the motion direction information carried by theta oscillation. Gamma oscillation is also important for feedforward transmission (Bastos et al., 2015; Vezoli et al., 2021). Although our experiment failed to find a significant change in the gamma band's decoding accuracy, it could be due to the limited signal-to-noise ratio of the MEG recording compared to that of the intracranial electrophysiological recording.

Inspired by the decoding finding in theta oscillation, we employed the GCA and uncovered an increase in the feedforward connection from EVC to V3A after VPL. Chen et al. (2015) reported that VPL optimized the feedforward connection from V3A to IPS. This discrepancy might arise from the recording technique difference (fMRI vs. MEG), as well as the methodological difference in the definition of IPS. Chen et al. (2015) used an fMRI localizer to define IPS, but we used an anatomically defined atlas instead. This resulted in the identification of a larger IPS region in our study. Both studies showed no post-training change in connection with MT+, which could be explained by the utilization of 100 % coherent RDKs and the V3A's dominant role in the local motion information processing over MT+ (Vaina et al., 2003; Cai et al., 2014).

What is beyond previous fMRI studies (e.g., Chen et al., 2015, 2017) is our study's temporally precise neural information.

Firstly, we found reduced decoding latency after VPL. This reduction was only found when classifying the trained direction from other directions. It has been shown that VPL reduces latencies of ERP components N170 (Su et al., 2012, 2013), P1 and P2 (Xi et al., 2020), and N1 (Ahmadi et al., 2018). The faster visual processing after VPL might arise from synaptic potentiation between neurons following visual experience (Grill-Spector et al., 2006). To our knowledge, our study is the first to reveal the VPL-induced change in decoding latency, which reflects the time when neural activity patterns for two or more visual stimuli become discriminable.

Secondly, the increase in feedforward connection from EVC to V3A was observed during 78–104 ms after the first RDK onset, indicating a change at an early stage of visual motion processing. Subsequently, the changes in decoding accuracy, cortical tuning, visual response in EVC, and feedforward connection co-occurred during 160–230 ms after the first RDK onset. In the time window of 160–230 ms after stimulus onset, several MEG/EEG studies have also identified neural responses to motion stimuli (Hoffmann et al., 1999; Kreegipuu and Allik, 2007; Kuba and Kubová, 1992; Kubová et al., 1990; Prieto et al., 2007). Specifically, a motion-onset visual evoked potential, N2, was observed 160–200 ms after motion onset (Bach and Ullrich, 1994; Kubová et al., 1995; Niedeggen and Wist, 1999). Thus, the VPL-induced changes in our results are likely to be associated with relatively early and feedforward processing of motion information.

Notably, the peak of motion direction decoding accuracy in our study was mainly reached between 160 and 230 ms after the first RDK onset. A correlation between the behavioral thresholds and the peak decoding accuracies was found across subjects in all three tests – Pre, Post1, and Post2. In other words, the MEG peak decoding accuracy in this time window could not only estimate the individual differences in vision before training but also parallel individual behavioral performance after training. Similarly, Gold and Shadlen (2001) found that the spike discharges in the superior colliculus and lateral intraparietal area (LIP), both occurring within 100–250 ms after the onset of motion stimuli, could accurately predict the sensory judgments in macaques. Taken together, these findings suggest that, for visual motion processing, neural activities within this period could mirror behavioral performance.

Our study found increased motion direction decoding accuracy, sharpened cortical tuning, enhanced EVC response, and enhanced feedforward connection from EVC to V3A during roughly the same period. These training-induced changes, while not correlated with each other, might reflect two key aspects of the neural mechanisms underpinning visual motion perceptual learning. First, training appears to improve sensory coding, as evidenced by the increased motion direction decoding accuracy, sharpened cortical tuning, and enhanced EVC response. Second, training could strengthen cortical-cortical connectivity that might be associated with perceptual decision-making, as indicated by the enhanced feedforward connection from EVC to V3A. Liu and Pack (2017) have found that training moves the readout of motion information between MT and lower-level cortical areas. Although Liu and Pack's findings are very interesting, due to the difference in training paradigm, their findings do not appear to be directly related to our findings.

Although we have observed performance improvements (i.e., learning effects) at the untrained directions, we failed to find corresponding changes in the decoding, IEM, GCA, or cortical activity analyses. One possible reason is that we limited our analysis to the 72 sensors covering the occipital lobe. However, direction non-specific learning may involve changes in task strategy, decision-making, and attentional allocation, which are likely associated with higher-order cortical areas (Kahnt et al., 2011; Law and Gold, 2009; Gilbert and Li, 2013; Li, 2016). Our study focused on direction-specific learning and its related neural activity in the visual cortex. The current analyses are not well-suited to investigate direction non-specific learning. We admit that this is a limitation of our study.

In this study, the gender ratio is not well-balanced, with fewer male subjects than female subjects. To our knowledge, very few studies have explored the gender difference in motion perception, especially motion perceptual learning, Murray et al. (2018) found that male subjects have significantly shorter motion duration thresholds than female subjects. McDevitt et al. (2014) discovered that male subjects exhibited more learning specificity than female subjects. This issue might be an interesting topic for future study.

To the best of our knowledge, this study is the first to make an exploration of the long-term neural mechanisms of visual motion perceptual learning using MEG. It provides new information that sheds light on the temporal characteristics of the VPL effects in the visual cortex. Future research could further explore this issue in human subjects, especially with the aid of deep neural networks (Wu and Liang, 2010; Wenliang and Seitz, 2018; Manenti et al., 2023) and intracranial recordings (e.g., stereoelectroencephalography, sEEG) that can provide

very precise spatial and temporal information.

Ethics statement

All subjects gave written, informed consent in accordance with the procedures and protocols approved by the human subject review committee of Peking University.

Data and code availability

Our analyses on MEG data were performed using the Brainstorm toolbox (Tadel et al., 2011) and the Neural Decoding Toolbox (Meyers, 2013) in MATLAB (MathWorks, Inc., Natick, Massachusetts). The data supporting the results reported in the study are available at https://github.com/WMSYQ/MEG_code. The data generated in this study are available from the corresponding author on reasonable request.

CRediT authorship contribution statement

Yongqian Song: Writing – review & editing, Writing – original draft, Visualization, Methodology, Investigation, Formal analysis, Data curation, Conceptualization. **Qian Wang:** Writing – review & editing, Supervision, Methodology, Funding acquisition, Data curation. **Fang Fang:** Writing – review & editing, Supervision, Resources, Project administration, Methodology, Funding acquisition, Data curation, Conceptualization.

Declaration of competing interest

The authors declare that they have no conflict of interest.

Acknowledgments

This work was supported by the National Science and Technology Innovation 2030 Major Program (2022ZD0204802, 2022ZD0204804), the National Natural Science Foundation of China (T2421004, 31930053, 32171039).

Supplementary materials

Supplementary material associated with this article can be found, in the online version, at doi:10.1016/j.neuroimage.2024.120897.

Data availability

Data will be made available on request.

References

Ahissar, M., Hochstein, S., 1997. Task difficulty and the specificity of perceptual learning. Nature 387 (6631), 401–406.
Ahmadi, M., McDevitt, E.A., Silver, M.A., Mednick, S.C., 2018. Perceptual learning induces changes in early and late visual evoked potentials. Vis. Res. 152, 101–109.
Akaike, H., 1974. A new look at the statistical model identification. IEEE Trans. Autom. Control 19 (6), 716–723.
Bach, M., Ullrich, D., 1994. Motion adaptation governs the shape of motion-evoked cortical potentials. Vis. Res. 34 (12), 1541–1547.
Ball, K., Sekuler, R., 1982. A specific and enduring improvement in visual motion discrimination. Science 218 (4573), 697–698.
Ball, K., Sekuler, R., 1987. Direction-specific improvement in motion discrimination. Vis. Res. 27 (6), 953–965.
Bao, M., Yang, L., Rios, C., He, B., Engel, S.A., 2010. Perceptual learning increases the strength of the earliest signals in visual cortex. J. Neurosc. 30 (45), 15080–15084.
Barnett, L., Seth, A.K., 2014. The MVGC multivariate Granger causality toolbox: a new approach to Granger-causal inference. J. Neurosci. Methods 223, 50–68.
Bastos, A.M., Vezoli, J., Bosman, C.A., Schoffelen, J.-M., Oostenveld, R., Dowdall, J.R., De Weerd, P., Kennedy, H., Fries, P., 2015. Visual areas exert feedforward and feedback influences through distinct frequency channels. Neuron 85 (2), 390–401.
Bejjanki, V.R., Beck, J.M., Lu, Z.-L., Pouget, A., 2011. Perceptual learning as improved probabilistic inference in early sensory areas. Nat. Neurosci. 14 (5), 642–648.
Bi, T., Chen, J., Zhou, T., He, Y., Fang, F., 2014. Function and structure of human left fusiform cortex are closely associated with perceptual learning of faces. Curr. Biol. 24 (2), 222–227.
Bi, T., Chen, N., Weng, Q., He, D., Fang, F., 2010. Learning to discriminate face views. J. Neurophysiol. 104 (6), 3305–3311.
Cai, P., Chen, N., Zhou, T., Thompson, B., Fang, F., 2014. Global versus local: double dissociation between MT+ and V3A in motion processing revealed using continuous theta burst transcranial magnetic stimulation. Exp. Brain Res. 232 (12), 4035–4041.
Chen, N., Bi, T., Zhou, T., Li, S., Liu, Z., Fang, F., 2015. Sharpened cortical tuning and enhanced cortico-cortical communication contribute to the long-term neural mechanisms of visual motion perceptual learning. Neuroimage 115, 17–29.
Chen, N., Lu, J., Shao, H., Weng, X., Fang, F., 2017. Neural mechanisms of motion perceptual learning in noise: motion perceptual learning in noise. Hum. Brain Mapp. 38 (12), 6029–6042.
Dale, A.M., Liu, A.K., Fischl, B.R., Buckner, R.L., Belliveau, J.W., Lewine, J.D., Halgren, E., 2000. Dynamic statistical parametric mapping: combining fMRI and MEG for high-resolution imaging of cortical activity. Neuron 26 (1), 55–67.
Ding, M., Bressler, S.L., Yang, W., Liang, H., 2000. Short-window spectral analysis of cortical event-related potentials by adaptive multivariate autoregressive modeling: data preprocessing, model validation, and variability assessment. Biol. Cybern. 83 (1), 35–45.
Dosher, B.A., Jeter, P., Liu, J., Lu, Z.-L., 2013. An integrated reweighting theory of perceptual learning. Proc. Natl. Acad. Sci. USA 110 (33), 13678–13683.
Dosher, B., Lu, Z.-L., 2017. Visual perceptual learning and models. Annu Rev. Vis. Sci. 3, 343–363.
Engemann, D.A., Gramfort, A., 2015. Automated model selection in covariance estimation and spatial whitening of MEG and EEG signals. Neuroimage 108, 328–342.
Fahle, M., Poggio, T. (Eds.), 2002. Perceptual Learning. MIT Press.
Florin, E., Gross, J., Pfeifer, J., Fink, G.R., Timmermann, L., 2010. The effect of filtering on Granger causality based multivariate causality measures. Neuroimage 50 (2), 577–588.
Furmanski, C.S., Schluppeck, D., Engel, S.A., 2004. Learning strengthens the response of primary visual cortex to simple patterns. Curr. Biol. 14 (7), 573–578.
Gibson, E.J., 1963. Perceptual learning. Annu. Rev. Psychol. 14 (1), 29–56.
Gold, J.I., Shadlen, M.N., 2001. Neural computations that underlie decisions about sensory stimuli. Trends Cogn. Sci. 5 (1), 10–16.
Gilbert, C.D., Li, W., 2013. Top-down influences on visual processing. Nat. Rev. Neurosci. 14 (5), 5.
Granger, C.W.J., 1969. Investigating causal relations by econometric models and cross-spectral methods. Econometrica 37 (3), 424–438.
Grill-Spector, K., Henson, R., Martin, A., 2006. Repetition and the brain: neural models of stimulus-specific effects. Trends Cogn. Sci. 10 (1), 14–23.
Gu, Y., Liu, S., Fetsch, C., Yang, Y., Fok, S., Sunkara, A., DeAngelis, G., Angelaki, D., 2011. Perceptual learning reduces interneuronal correlations in macaque visual cortex. Neuron 71 (4), 750–761.
Hämäläinen, M., Hari, R., Ilmoniemi, R.J., Knuutila, J., Lounasmaa, O.V., 1993. Magnetoencephalography theory, instrumentation, and applications to noninvasive studies of the working human brain. Rev. Mod. Phys. 65 (2), 413–497.
He, Q., Yang, X.-Y., Gong, B., Bi, K., Fang, F., 2022. Boosting visual perceptual learning by transcranial alternating current stimulation over the visual cortex at alpha frequency. Brain Stimul. 15 (3), 546–553.
Hoffmann, M., Dorn, T.J., Bach, M., 1999. Time course of motion adaptation: motion-onset visual evoked potentials and subjective estimates. Vis. Res. 39 (3), 437–444.
Hua, T., Bao, P., Huang, C.-B., Wang, Z., Xu, J., Zhou, Y., Lu, Z.-L., 2010. Perceptual learning improves contrast sensitivity of V1 neurons in cats. Curr. Biol. 20 (10), 887–894.
Huang, M.X., Mosher, J.C., Leahy, R.M., 1999. A sensor-weighted overlapping-sphere head model and exhaustive head model comparison for MEG. Phys. Med. Biol. 44 (2), 423–440.
Hubel, D.H., Wiesel, T.N., 1962. Receptive fields, binocular interaction and functional architecture in the cat's visual cortex. J. Physiol. 160 (1), 106–154.
Hubel, D.H., Wiesel, T.N., 1968. Receptive fields and functional architecture of monkey striate cortex. J. Physiol. 195 (1), 215–243.
Isik, L., Meyers, E.M., Leibo, J.Z., Poggio, T., 2014. The dynamics of invariant object recognition in the human visual system. J Neurophysiol. 111 (1), 91–102.
Jing, R., Yang, C., Huang, X., Li, W., 2021. Perceptual learning as a result of concerted changes in prefrontal and visual cortex. Curr. Biol. 31 (20), 4521–4533 e3.
Kahnt, T., Grueschow, M., Speck, O., Haynes, J.-D., 2011. Perceptual learning and decision-making in human medial frontal cortex. Neuron 70 (3), 549–559.
Karni, A., Sagi, D., 1991. Where practice makes perfect in texture discrimination: evidence for primary visual cortex plasticity. Proc. Natl. Acad. Sci. USA 88 (11), 4966–4970.
Karni, A., Sagi, D., 1993. The time course of learning a visual skill. Nature 365 (6443), 250–252.
Kienitz, R., Cox, M.A., Dougherty, K., Saunders, R.C., Schmiedt, J.T., Leopold, D.A., Maier, A., Schmid, M.C., 2021. Theta, but not gamma oscillations in area V4 depend on input from primary visual cortex. Curr. Biol. 31 (3), 635–642 e3.
Kreegipuu, K., Allik, J., 2007. Detection of motion onset and offset: reaction time and visual evoked potential analysis. Psychol. Res. 71 (6), 703–708.
Kuba, M., Kubová, Z., 1992. Visual evoked potentials specific for motion onset. Doc. Ophthalmol. 80 (1), 83–89.
Kubová, Z., Kuba, M., Hubacek, J., VíT, F., 1990. Properties of visual evoked potentials to onset of movement on a television screen. Doc. Ophthalmol. 75 (1), 67–72.
Kubová, Z., Kuba, M., Spekreijse, H., Blakemore, C., 1995. Contrast dependence of motion-onset and pattern-reversal evoked potentials. Vis. Res. 35 (2), 197–205.

Larcombe, S.J., Kennard, C., Bridge, H., 2018. Increase in MST activity correlates with visual motion learning: a functional MRI study of perceptual learning: functional MRI study of perceptual learning. Hum. Brain Mapp. 39 (1), 145–156.
Law, C.-T., Gold, J.I., 2009. Reinforcement learning can account for associative and perceptual learning on a visual-decision task. Nat. Neurosci. 12 (5), 655–663.
Lewis, C.M., Baldassarre, A., Committeri, G., Romani, G.L., Corbetta, M., 2009. Learning sculpts the spontaneous activity of the resting human brain. Proc. Natl. Acad. Sci. 106 (41), 17558–17563.
Li, W., 2016. Perceptual learning: use-dependent cortical plasticity. Annu Rev. Vis. Sci. 2 (1), 109–130.
Liu, L.D., Pack, C.C., 2017. The contribution of area MT to visual motion perception depends on training. Neuron 95 (2), 436–446 e3.
Liu, Z., Weinshall, D., 2000. Mechanisms of generalization in perceptual learning. Vis. Res. 40 (1), 97–109.
Lu, J., Luo, L., Wang, Q., Fang, F., Chen, N., 2021. Cue-triggered activity replay in human early visual cortex. Sci. China Life Sci. 64, 144–151.
Luo, L., Wang, X., Lu, J., Chen, G., Luan, G., Li, W., Wang, Q., Fang, F., 2023. Local field potentials, spiking activity, and receptive fields in human visual cortex. Sci. China Life Sci. 67, 543–554.
Manenti, G.L., Dizaji, A.S., Schwiedrzik, C.M., 2023. Variability in training unlocks generalization in visual perceptual learning through invariant representations. Curr. Biol. 33 (5), 817–826 e3.
McDevitt, E.A., Rokem, A., Silver, M.A., Mednick, S.C., 2014. Sex differences in sleep-dependent perceptual learning. Vis. Res. 99, 172–179.
Meyers, E.M., 2013. The neural decoding toolbox. Front. Neuroinform 7 (8).
Mo, C., Lu, J., Wu, B., Jia, J., Luo, H., Fang, F., 2019. Competing rhythmic neural representations of orientations during concurrent attention to multiple orientation features. Nat. Commun. 10 (1), 5264.
Mukai, I., Kim, D., Fukunaga, M., Japee, S., Marrett, S., Ungerleider, L.G., 2007. Activations in visual and attention-related areas predict and correlate with the degree of perceptual learning. J. Neurosci. 27 (42), 11401–11411.
Murray, S.O., Schallmo, M.-P., Kolodny, T., Millin, R., Kale, A., Thomas, P., Rammsayer, T.H., Troche, S.J., Bernier, R.A., Tadin, D., 2018. Sex differences in visual motion processing. Curr. Biol. 28 (17), 2794–2799 e3.
Niedeggen, M., Wist, E.R., 1999. Characteristics of visual evoked potentials generated by motion coherence onset. Cogn. Brain Res. 8 (2), 95–105.
Prieto, E.A., Barnikol, U.B., Soler, E.P., Dolan, K., Hesselmann, G., Mohlberg, H., Amunts, K., Zilles, K., Niedeggen, M., Tass, P.A., 2007. Timing of V1/V2 and V5+ activations during coherent motion of dots: an MEG study. Neuroimage 37 (4), 1384–1395.
Raiguel, S., Vogels, R., Mysore, S.G., Orban, G.A., 2006. Learning to see the difference specifically alters the most informative V4 neurons. J. Neurosci. 26 (24), 6589–6602.
Ramkumar, P., Jas, M., Pannasch, S., Hari, R., Parkkonen, L., 2013. Feature-specific information processing precedes concerted activation in human visual cortex. J. Neurosci. 33 (18), 7691–7699.
Schoups, A.A., Vogels, R., Orban, G.A., 1995. Human perceptual learning in identifying the oblique orientation: retinotopy, orientation specificity and monocularity. J. Physiol. 483 (3), 797–810.
Schoups, A., Vogels, R., Qian, N., Orban, G., 2001. Practising orientation identification improves orientation coding in V1 neurons. Nature 412 (6846), 549–553.
Schwartz, S., Maquet, P., Frith, C., 2002. Neural correlates of perceptual learning: a functional MRI study of visual texture discrimination. Proc. Natl. Acad. Sci. 99 (26), 17137–17142.
Shibata, K., Chang, L.-H., Kim, D., Náñez, J.E., Kamitani, Y., Watanabe, T., Sasaki, Y., 2012. Decoding reveals plasticity in V3A as a result of motion perceptual learning. PLoS One 7 (8), e44003.
Shiu, L.-P., Pashler, H., 1992. Improvement in line orientation discrimination is retinally local but dependent on cognitive set. Percept. Psychophys. 52 (5), 582–588.
Sprague, T.C., Adam, K.C.S., Foster, J.J., Rahmati, M., Sutterer, D.W., Vo, V.A., 2018. Inverted encoding models assay population-level stimulus representations, not single-unit neural tuning. eNeuro 5 (3) ENEURO.0098-18.2018. 1-5.
Spyropoulos, G., Bosman, C.A., Fries, P., 2018. A theta rhythm in macaque visual cortex and its attentional modulation. Proc. Natl. Acad. Sci. 115 (24), E5614–E5623.
Su, J., Chen, C., He, D., Fang, F., 2012. Effects of face view discrimination learning on N170 latency and amplitude. Vis. Res. 61, 125–131.
Su, J., Tan, Q., Fang, F., 2013. Neural correlates of face gender discrimination learning. Exp. Brain Res. 225 (4), 569–578.
Tadel, F., Baillet, S., Mosher, J.C., Pantazis, D., Leahy, R.M., 2011. Brainstorm: A user-friendly application for MEG/EEG analysis. Comput. Intell. Neurosci. 2011 (1687–5265), 1–13.
Taulu, S., Kajola, M., 2005. Presentation of electromagnetic multichannel data: the signal space separation method. J. Appl. Phys. 97 (12): 124905, 1-10.
Vaina, L.M., Gryzwacz, N.M., Saiviroonporn, P., LeMay, M., Bienfang, D.C., Cowey, A., 2003. Can spatial and temporal motion integration compensate for deficits in local motion mechanisms? Neuropsychologia 41 (13), 1817–1836.
Vezoli, J., Vinck, M., Bosman, C.A., Bastos, A.M., Lewis, C.M., Kennedy, H., Fries, P., 2021. Brain rhythms define distinct interaction networks with differential dependence on anatomy. Neuron 109 (23), 3862–3878.e5.
Wang, L., Mruczek, R.E.B., Arcaro, M.J., Kastner, S., 2015. Probabilistic maps of visual topography in human cortex. Cereb. Cortex 25 (10), 3911–3931.
Watanabe, T., Sasaki, Y., 2015. Perceptual learning: toward a comprehensive theory. Annu. Rev. Psychol. 66 (1), 197–221.
Watson, A.B., Pelli, D.G., 1983. Quest: a Bayesian adaptive psychometric method. Percept. Psychophys. 33 (2), 113–120.
Wenliang, L.K., Seitz, A.R., 2018. Deep neural networks for modeling visual perceptual learning. J. Neurosci. 38 (27), 6028–6044.
Wu, S., Liang, P., 2010. Computational neuroscience in China. Sci. China Life Sci. 53 (3), 385–397.
Xi, J., Zhang, P., Jia, W.-L., Chen, N., Yang, J., Wang, G.-T., Dai, Y., Zhang, Y., Huang, C.-B., 2020. Multi-stage cortical plasticity induced by visual contrast learning. Front. Neurosci. 14 (555701), 1–15.
Yan, Y., Rasch, M.J., Chen, M., Xiang, X., Huang, M., Wu, S., Li, W., 2014. Perceptual training continuously refines neuronal population codes in primary visual cortex. Nat. Neurosci. 17 (10), 1380–1387.
Yang, T., 2004. The effect of perceptual learning on neuronal responses in monkey visual area V4. J. Neurosci. 24 (7), 1617–1626.
Yotsumoto, Y., Chang, L., Watanabe, T., Sasaki, Y., 2009. Interference and feature specificity in visual perceptual learning. Vis. Res. 49 (21), 2611–2623.
Yotsumoto, Y., Watanabe, T., Sasaki, Y., 2008. Different dynamics of performance and brain activation in the time course of perceptual learning. Neuron 57 (6), 827–833.
Zhang, Y., Bi, K., Li, J., Wang, Y., Fang, F., 2023. Dyadic visual perceptual learning on orientation discrimination. Curr. Biol. 33 (12), 2407–2416 e4.
Zohary, E., Celebrini, S., Britten, K., Newsome, W., 1994. Neuronal plasticity that underlies improvement in perceptual performance. Science 263 (5151), 1289–1292.